Journal of Nuclear Medicine, published on April 9, 2021 as doi:10.2967/jnumed.120.259325

Longitudinal imaging of T-cells and inflammatory demyelination in a preclinical model of multiple sclerosis using ^{18}F-FAraG PET and MRI

Authors

Caroline Guglielmetti[1,2], Jelena Levi[3], Tony L. Huynh[2], Brice Tiret[1,2], Joseph Blecha[2], Ryan Tang[2], Henry VanBrocklin[2], Myriam M. Chaumeil[1,2]

Affiliations

[1] Department of Physical Therapy and Rehabilitation Science, University of California, San Francisco, CA, USA

[2] Department of Radiology and Biomedical Imaging, University of California, San Francisco, CA, USA

[3] CellSight Technologies, Inc.

Corresponding Authors

Caroline Guglielmetti, Ph.D.,

Department of Physical Therapy and Rehabilitation Science, University of California San Francisco, 1700 4th Street, BH 204, Mission Bay Campus, San Francisco, CA 94143.

Email: caroline.guglielmetti@ucsf.edu

Myriam M. Chaumeil, Ph.D.,

Department of Physical Therapy and Rehabilitation Science, University of California San Francisco, 1700 4th Street, BH 204, Mission Bay Campus Box 2530, San Francisco, CA 94143.

Email: myriam.chaumeil@ucsf.edu

Word Count: 4,991

Financial Support

This work was supported by research grants: NIH R21AI153749, NIH R01NS102156, NMSS research grant RG-1701-26630, Hilton Foundation – Marilyn Hilton Award for Innovation in MS Research #17319 and the Dana Foundation: The David Mahoney Neuroimaging program. J. Levi is employed by CellSight Technologies. CellSight Technologies is commercializing ^{18}F-FAraG as a PET tracer for evaluation of immune response in immunotherapy. No other potential conflicts of interest relevant to this article exist.

Short Running Title: Imaging CNS T-cells with ^{18}F-FAraG

ABSTRACT

Lymphocytes and innate immune cells are key drivers of multiple sclerosis (MS) and are the main target of MS disease modifying therapies (DMT). *Ex vivo* analyses of MS lesions have revealed cellular heterogeneity and variable T-cell levels, which may have important implication for patient stratification and choice of DMT. Although magnetic resonance imaging (MRI) has proven valuable to monitor DMT efficacy, its lack of specificity for cellular subtypes highlights the need for complementary methods to improve lesion characterization. Here, we evaluated the potential of 2'-deoxy-2'-[^{18}F]fluoro-9-β-D-arabinofuranosylguanine (^{18}F-FAraG) PET imaging to non-invasively assess infiltrating T-cells and to provide, in combination with MRI, a novel tool to determine lesion types.

Methods

We used a novel MS mouse model that combines cuprizone and experimental autoimmune encephalomyelitis (EAE) to reproducibly induce two brain inflammatory lesion types, differentiated by their T-cell content. ^{18}F-FAraG PET imaging, T_2-weighted MRI, and T_1-weighted contrast-enhanced MRI were performed prior to disease induction, during demyelination with high levels of innate immune cells, and following T-cell infiltration. Fingolimod immunotherapy was used to evaluate the ability of PET and MRI to detect therapy response. *Ex vivo* immunofluorescence analyses for T-cells, microglia/macrophages, myelin and blood brain barrier (BBB) integrity were performed to validate the *in vivo* findings.

Results

^{18}F-FAraG signal was significantly increased in brain and spinal cord at the time point of T-cell infiltration. ^{18}F-FAraG signal from white matter (corpus callosum), and grey matter (cortex, hippocampus) further correlated with T-cell density. T_2-weighted MRI detected white matter lesions independently of T-cells. T_1-weighted contrast-enhanced MRI indicated BBB disruption at the time point of T-cell infiltration. Fingolimod treatment prevented motor deficits and decreased T-cell and microglia/macrophage levels. In agreement, ^{18}F-FAraG signal was decreased in brain and spinal cord of Fingolimod-treated mice, T_1-weighted contrast-enhanced MRI revealed intact BBB, while T_2-weighted MRI remained unchanged.

Conclusion

The combination of MRI and ^{18}F-FAraG PET enables detection of inflammatory demyelination and T-cell infiltration in a MS mouse model, providing a new way to evaluate lesion heterogeneity during disease progression and following DMT. Upon clinical translation, these methods hold great potential for patient stratification, monitoring MS progression and therapy responses.

KEY WORDS

T-cells; multiple sclerosis; central nervous system; ^{18}F-FAraG PET imaging; MRI

INTRODUCTION

Adaptive and innate immune cells play a critical role in the onset and progression of multiple sclerosis (MS) (*1*). Currently, all disease modifying therapies (DMT) that slow down MS progression act on the immune system (*2*). Evidence from histopathology analysis of brain tissue indicate that lesions are heterogeneous and T-cell concentrations are highly variable at sites of active demyelination (*3-7*). Although conventional MRI is well-established to diagnose and monitor MS progression by detecting lesions, its inability to provide specific information on underlying cellular events justifies the development of new complementary tools to improve lesion characterization (*8,9*). Briefly, T_1-weighted contrast-enhanced MRI and T_2-weighted MRI can assess blood brain barrier (BBB) integrity and demyelination and/or inflammation, respectively, but are unable to inform on immune cell types presence (*1,9*). Imaging of immune cells would improve our understanding of lesion progression across the course of MS, and most importantly, allow for proper stratification of patients and optimized choice of therapeutic regimen.

Recently, molecular imaging using novel tracers for positron emission tomography (PET) have enabled the *in situ* detection of T-cells in living organisms. Upon transport inside the cell by nucleoside transporters, 2'-deoxy-2'-[^{18}F]fluoro-9-β-D-arabinofuranosylguanine (^{18}F-FAraG) is phosphorylated by cytoplasmic deoxycytidine and mitochondrial deoxyguanosine kinases (*10*), trapping this PET probe in the cell. ^{18}F-FAraG PET has shown high specificity for activated T-cells *in vitro* and in models of graft-versus-host disease, inflammatory arthritis and cancer (*10-14*), and is currently under investigation in clinical trials. Because MS lesions may differ in their T-cell accumulation, ^{18}F-FAraG PET appears as a complementary method to assess lesion types in MS.

The novel cuprizone and experimental autoimmune encephalomyelitis (CPZ-EAE) model for MS (*15*) presents two types of brain lesions temporally distinct and highly reproducible. First, cuprizone administration induces demyelination and elevated microglia/ macrophages. Next, following EAE immunization these lesions additionally display T-cell infiltration.

Here, we investigated the potential of ^{18}F-FAraG PET to detect T-cell infiltration into the CNS in the CPZ-EAE model of MS. We also evaluated the ability of ^{18}F-FAraG PET to detect response to Fingolimod, a DMT which limits the infiltration of T-cells into the CNS (*16*). Our findings showed that MRI allowed the detection of inflammatory demyelination independently of T-cell presence, while ^{18}F-FAraG PET enabled lesion stratification by informing on T-cell load, thus providing a novel methodology to evaluate immune cell heterogeneity in lesions.

MATERIALS AND METHODS

Animals and Experimental Design

All animal research was approved by the Institutional Animal Care and Use Committee of the University of California San Francisco. Induction of the CPZ-EAE model was achieved by feeding eight-week-old C57BL/6J female mice (n = 32, Jackson Laboratories, ME, USA) mice a CPZ supplemented diet (0.25%, Sigma) for three weeks, followed by two weeks of normal chow. At the start of the sixth week, mice were immunized with myelin oligodendrocyte glycoprotein (MOG_{35-55}) in complete Freund's adjuvant. Mice received an intraperitoneal injection of pertussis toxin on the day of immunization and the following day (Hooke Laboratories). Following immunization, mice were evaluated daily for motor symptoms, and scored using a EAE scale as previously described (*17*). A first group of control mice underwent a 60-minute dynamic PET acquisition (n=4) immediately followed by *ex vivo* biodistribution studies to evaluate tracer distribution and accumulation. A second group of CPZ-EAE mice (n=10) underwent longitudinal PET and MR imaging sessions at the following time points: prior to disease induction (Baseline), after three weeks of cuprizone (W3), and at the end of the seventh week which corresponds to 14±1 days post-immunization (W7-14dpi). Euthanasia was performed after the last imaging session. A third group of CPZ-EAE mice (n=10) received a daily administration of a Fingolimod solution by oral gavage (0.3 mg/kg, Combi-Blocks) for 14±1 dpi, starting on the day of immunization. PET and MR imaging were performed at W7-14dpi and immediately followed by euthanasia. A fourth group of mice that did not undergo any imaging procedures was used for histological analyses (n=4 control, n=4 W3 CPZ). Experimental outline is shown in Supplemental Figure 1.A.

Magnetic Resonance Imaging Acquisition

All *in vivo* MR experiments were conducted on a 14.1 Tesla vertical MR system (Agilent Technologies) equipped with 100 G/cm gradients and a ^{1}H volume coil (ØI=40 mm). For each imaging session, mice were anesthetized using isoflurane (1.5–2% in O_2) and a 27-gauge catheter was placed in the tail vein for intravenous (iv) injection of the gadolinium contrast agent (Gadavist, Bayer). Animals were placed in a water heated cradle with the head secured to ensure similar positioning between experiments. Respiration was continuously monitored using PC-SAM software. T_2-weighted MRI was acquired using the following parameters: TE/TR = 11.8/3000 ms, RARE factor = 8, slice thickness = 0.5 mm, gap = 0.25 mm, number of averages = 6, matrix = 256×256, and field of view (FOV) = 30×30 mm^2. T_1-weighted MRI was acquired prior and two minutes after injection of Gadavist bolus (1 mmol/kg of body weight) using TE/TR = 2.09/120 ms, slice thickness = 0.8 mm, gap = 0.2 mm, number of averages = 10, matrix = 256×256, and FOV = 20×20 mm^2.

Positron Emission Tomography Acquisition

All *in vivo* PET/ computerized tomography (CT) scans were performed on a dedicated small animal PET/ CT scanner (Inveon, Siemens Healthcare, Malvern, PA, USA). ^{18}F-FAraG was synthesized as previously described (*11*). Mice were anesthetized using isoflurane (2% in O_2) and ^{18}F-FAraG (3.7–5.5 MBq in 100-200 µL saline) was injected into a catheterized tail vein. Following ^{18}F-FAraG injection, mice were either imaged immediately for 60 minutes, or recovered from anesthesia and were ambulatory for 60 minutes to permit tracer distribution, and whole-body static scans (15 minutes PET acquisition followed by CT scan for anatomic reference and attenuation correction) were then performed under anesthesia using isoflurane (2% in O_2) with warming and constant monitoring. PET images were reconstructed using the ordered subsets expectation maximization algorithm provided by the manufacturer.

***Ex vivo* Biodistribution Studies**

Immediately after dynamic PET acquisitions control mice (n=4) were euthanized and blood and brain were collected. The blood and brain tissue were weighed and radioactivity measured using a Hidex AMG gamma counter. The % injected dose per gram of tissue (% ID/g) was calculated against a standard of known activity.

Magnetic Resonance Imaging and Positron Emission Tomography Analyses

Manual delineation of the corpus callosum, hippocampus, and cortex were performed on T_2-weighted images using AMIRA software, as indicated in Supplemental Figure 1.B. Normalized mean T_2-weighted signal intensity for each region of interest (ROI) was calculated as previously described (*18*). Whole brain alteration of the BBB was assessed by manually delineating hyperintense regions on post-contrast T_1-weighted images as shown in Supplemental Figure 1.C. To investigate regional differences in the PET signal throughout the brain, we co-registered PET/ CT images with T_2-weighted MR images using VivoQuant 4.0 patch3 software (Invicro). Partial volume correction was not performed. ROIs were manually delineated over the entire brain, corpus callosum, hippocampus and cortex on T_2-weighted images, and corresponding mean PET signal values, expressed as % ID/g, were calculated for each ROI. In addition, we manually delineated the cervical/ thoracic and lumbar spinal cord segments as described by James et al. (*19*), and the subiliac lymph nodes, to obtain the corresponding mean % ID/g values (Supplemental Figure 1.D).

Immunofluorescence Analyses

All analyses were performed as previously described (*17*), except for the inclusion of CD3 and fibrinogen immunostaining using the following combinations: rabbit anti-fibrinogen (A0080, 1:200 dilution; Dako)

with donkey anti-rabbit Alexa Fluor 555 (A31572, 1:600 dilution; Invitrogen); rat anti-CD3 (MCA500G, 1: 400 dilution; BioRad) with goat anti-rat Alexa Fluor 488 (A11006, 1:800 dilution; Invitrogen). Quantitative analyses of immunofluorescence images were performed using NIH ImageJ (v1.52p). CD3 cell number was manually evaluated using the Cell Counter tool from multiple regions depicted in Supplemental Figure 1.E. Macrophages/microglia (Iba1), myelin basic protein (MBP), and fibrinogen levels were determined based on image-covering staining and expressed as percentage of the total area (*17*).

Statistical Analyses

Data are reported as mean ± standard error. Dots represent the mean value obtained for each individual and lines indicate longitudinal measurements. Statistical analyses of longitudinal *in vivo* PET and MRI were performed using a mixed-effect model with the restricted maximum likelihood method (GraphPad Prism version 8.4.3). A One-Way ANOVA was used to assess statistical significance of the MBP, Iba1, CD3 and fibrinogen immunofluorescence staining. Correlation analyses were performed using the Pearson correlation coefficient. P-values were corrected for multiple testing using the Tukey post-hoc test (*$*p \leq 0.05$, **$p \leq 0.01$, ***$p \leq 0.001$, ****$p \leq 0.0001$).

RESULTS

^{18}F-FAraG PET and MRI Detect T-cells and Inflammatory Demyelination in the CPZ-EAE Mouse Brain

Dynamic ^{18}F-FAraG PET acquisitions in control animals revealed a steady increase in ^{18}F-FAraG signal in the brain over 60 minutes. Brain-to-blood ratio calculated from PET images (over last 10 minutes) was 1.1±0.2, and brain-to-blood ratio calculated from subsequent *ex vivo* biodistribution studies was 0.73±0.1 (Supplemental Figure 2). These results indicate that ^{18}F-FAraG accumulates in the brain and crosses the intact BBB in mice. Next, we evaluated the potential of ^{18}F-FAraG PET to detect brain infiltrating T-cells in the CPZ-EAE model. Figure 1.A shows PET/ CT images obtained from the mouse brain and a clear increase of ^{18}F-FAraG signal in the corpus callosum and hippocampal area at W7-14dpi. Quantitative analyses revealed that ^{18}F-FAraG signal was significantly increased in the entire brain after immunization at W7-14dpi ($p=0.0004$ and $p=0.038$ compared to baseline and W3, respectively). A significant ^{18}F-FAraG signal increase was also seen in the corpus callosum ($p=0.0003$ and $p=0.0097$ compared to baseline and W3, respectively) and hippocampus at W7-14dpi ($p=0.0005$ and $p=0.007$ compared to baseline and W3, respectively). Higher ^{18}F-FAraG signal was found in the somatosensory cortex ($p=0.0077$ compared to baseline). Histological analyses confirmed significant increase of CD3 T-cells after immunization at W7-14dpi, with the highest CD3 T-cells density in the hippocampus ($p<0.0001$ compared to both baseline and W3) followed by corpus callosum ($p=0.0006$ and $p=0.0007$ compared to baseline and W3, respectively) and cortex ($p=0.004$ and $p=0.0041$ compared to baseline and W3, respectively), in line with the PET imaging results (Figure 1.B). Also, in line with the imaging data, T-cell levels were not significantly increased in any region at W3 (Supplemental Figure 3). Analysis revealed a significant positive correlation between ^{18}F-FAraG uptake and CD3 T-cell number (Figure 1.C, r^2=0.72, $p<0.0001$).

Next, we assessed the potential of MRI to detect brain alteration at W3 and W7-14dpi during inflammatory demyelination. A leaky BBB was observed after immunization (W7-14dpi) (Figure 2, $p=0.0418$ and $p=0.05$ compared to Baseline and W3, respectively). The volume of T_1 enhancing lesion varied greatly between animals, ranging from 13 to 117 mm^3. T_2-weighted MRI detected the presence of hyperintense lesions in the corpus callosum after CPZ diet (W3, $p=0.0009$) and immunization (W7-14dpi, $p=0.0011$), but not in the hippocampus or cortex.

Inflammatory demyelination at W3 and W7-14dpi was confirmed by immunofluorescence analysis. Innate immune cells (Iba1) were significantly increased at W3 ($p<0.0001$) and W7-14dpi ($p<0.0001$) in the corpus callosum**,** along with demyelination (MBP) at W3 ($p<0.0001$) and W7-14dpi ($p=0.0059$) (Figure 3). Fibrinogen staining confirmed BBB disruption at W7-14dpi ($p=0.0353$ compared to both Baseline and W3). Similarly, increase in innate immune cells (Iba1) was observed at W3 and W7-

14dpi in the hippocampus *(p=0.0309* and *p=0.0002* compared to Baseline), and at W7-14dpi in the cortex *(p<0.0001* compared to Baseline) (Supplemental Figure 4). Interestingly, demyelination (MBP) was present at W3 in the hippocampus *(p=0.0117* compared to Baseline) and W7-14dpi in the cortex *(p=0.0048* and *p=0.0158*, compared to Baseline and W3, respectively). Fibrinogen staining confirmed BBB breakdown in the hippocampus at W7-14dpi *(p=0.0004* and *p=0.0002* compared to Baseline and W3, respectively*)*.

^{18}F-FAraG PET Detects T-cells in the Spinal Cord and Lymph Nodes

Following immunization, mice showed phenotypical symptoms of EAE pathology indicative of spinal cord lesions (mean EAE score: 2.2±0.3 at W7-14dpi). As shown in Figure 4.A, a clear ^{18}F-FAraG signal arising from the lumbar spinal cord can be observed at W7-14dpi. Quantitative analyses revealed significant increase of ^{18}F-FAraG signal in both cervical/ thoracic (*p<0.0001* and *p=0.0081* compared to Baseline and W3, respectively) and lumbar (*p<0.0001* and *p=0.0068* compared to Baseline and W3, respectively) spinal cord at W7-14dpi. CD3 T-cells were detected at W7-14dpi in cervical/ thoracic (*p<0.0001* and *p<0.0001* compared to Baseline and W3, respectively) and lumbar (*p<0.0001* and *p<0.0001* compared to Baseline and W3, respectively) spinal cord (Figure 4.B) and significantly correlated with ^{18}F-FAraG signal (Figure 4.C, r^2=0.78, *p=0.004*). ^{18}F-FAraG signal was also increased in the subiliac lymph nodes at W7-14dpi (*p<0.0001* and *p=0.0084* compared to Baseline and W3, respectively), in agreement with elicited adaptive immune response following immunization (Figure 5).

^{18}F-FAraG PET Detects Response to Fingolimod Therapy

We evaluated whether ^{18}F-FAraG could detect the effect of Fingolimod treatment. As mentioned above, untreated animals showed weakness/ paralysis of limbs (mean EAE score at W7-14dpi = 2.2±0.3). In contrast, Fingolimod-treated mice did not show any sign of EAE pathology (mean EAE score at W7-14dpi = 0±0) confirming the effect of Fingolimod treatment.

^{18}F-FAraG signal was significantly lower in the entire brain (*p=0.0467*), corpus callosum (*p=0.0011)*, hippocampus (*p=0.0169*) and cortex (*p=0.0355*) of Fingolimod-treated animals (Figure 6.A). No T_1 enhancing lesions could be detected in the brain of Fingolimod-treated mice (*p<0.0001,* Figure 6.B). Interestingly, T_2-weighted MRI did not detect any differences between Fingolimod-treated and untreated mice. Histological analyses confirmed significant lower CD3 T-cell number in the corpus callosum (*p=0.0047*), hippocampus (*p<0.0001*) and cortex (*p=0.0077*) following Fingolimod treatment (Figure 6.C, Supplemental Figure 5). Microglia and macrophages levels (Iba1) were decreased in Fingolimod-treated mice, while demyelination (MBP) was comparable between Fingolimod-treated and untreated animals.

Furthermore, ^{18}F-FAraG signal was significantly lower in the spinal cord and lymph nodes of Fingolimod-treated mice (Supplemental Figure 6).

DISCUSSION

Non-invasive visualization of immune cells within the CNS would tremendously help improving the diagnosis and monitoring of neurodegenerative disorders, particularly MS. Here, we showed the high potential of ^{18}F-FAraG PET for the detection of T-cell infiltration and accumulation within the CNS and lymphoid tissue in a MS model, and demonstrated its ability to detect response to an immunomodulatory DMT.

The CPZ-EAE model was particularly suited for this study as it allows evaluation of two lesion types well separated in time (W3 and W7-14dpi) within the same animal. Furthermore, in space, the differential load of T-cells throughout the brain, with different levels in white and grey matter, enables to evaluate the capability of ^{18}F-FAraG PET to detect various levels of infiltrating T-cells. We showed that ^{18}F-FAraG signal was strongly associated with T-cell density in brain and spinal cord. Prior *in vitro* studies have shown that ^{18}F-FAraG uptake also occurs in macrophages, but the agent is not retained due to low levels of cytoplasmic deoxycytidine and deoxyguanosine kinases (*10*). This is likely the case in our study as high level of microglia/macrophages are observed following cuprizone diet (W3) (*18*) but ^{18}F-FAraG signal remained unchanged compared to Baseline.

In healthy conditions, the adult brain has limited capacity for *de novo* synthesis of nucleosides and relies on uptake through nucleosides transporters present on the BBB, thus providing a means for ^{18}F-FAraG delivery to the brain (*20*). Although ^{18}F-FAraG low brain background signal enables detection of small changes in tracer accumulation (*11*), we noted higher ^{18}F-FaraG signal in ventral brain areas (Supplemental Figure 7). ^{18}F-FAraG brain uptake in the two cohorts of control mice showed different values (Figure 1, Supplemental Figure 2), which might be explained by different anesthesia lengths and/or acquisition parameters (static vs. dynamic). When normalizing ^{18}F-FAraG brain uptake to ^{18}F-FAraG uptake in muscle, no significant differences between these cohorts were found (Supplemental Figure 8).

In CPZ-EAE, increase of ^{18}F-FAraG signal coincided with the time point of BBB disruption measured by post-contrast T_1 MRI and fibrinogen immunostaining, which may facilitate ^{18}F-FAraG accumulation in the brain. However, we showed in Supplemental Figure 9 that T_1 enhancing lesion volumes did not correlate to ^{18}F-FAraG signal, and that ^{18}F-FAraG signal was increased in non-enhancing T_1 lesions containing high levels of CD3 T-cells. These findings further support that ^{18}F-FAraG provides additional information with regard to T-cell accumulation. Discrepancies between imaging modalities might also be explained by differences in molecular weight and lipid solubility of the different agents used to evaluate BBB permeability (*21*), although fibrinogen and Gadavist are well-established. Additionally, small lesions might remain undetected due to MRI resolution and partial volume effect.

Recent work by Chen *et al.* described 1-(2'-deoxy-2'-^{18}F-fluoroarabinofuranosyl) cytosine (^{18}F-FAC) use in the EAE model (*22*). ^{18}F-FAC has been shown to accumulate in leukocytes through

cytoplasmic deoxycytidine kinase phosphorylation in models of immune activation (*23,24*) and accumulated in nearly equal amount within brain-infiltrating T-cells and innate immune cells. When compared to our study, ^{18}F-FAC and ^{18}F-FAraG showed similar magnitude of change, displaying a 180% and 140% increase of brain PET signal compared to control mice, respectively, although the MS models were different. Similarly, following Fingolimod therapy, ^{18}F-FAC accumulation was decreased by 37% and ^{18}F-FAraG accumulation by 32% in the corpus callosum. Although Fingolimod blocks egress of lymphocytes out of secondary lymphoid organs (*16*), we observed lower ^{18}F-FAraG uptake in lymph nodes. This may be explained by Fingolimod's inhibition of T-cell activation (*25*) and will require further investigation in future studies. Surprisingly, in contrast with our findings, ^{18}F-FAC did not accumulate in the spinal cord, despite high T-cell levels and macrophage infiltration (*26*). This result was explained by low spinal cord cytoplasmic deoxycytidine kinase expression, and thus suggests that ^{18}F-FAraG might provide a more accurate detection of T-cells due to its higher affinity for deoxyguanosine kinase. Additionally, ^{18}F-FAC is deaminated in humans, limiting its clinical translation. In contrast, ^{18}F-FAraG has shown feasibility and safety in humans (*11*), and is under investigation in multiple clinical trials.

Alongside PET, conventional MRI proved essential to detect brain lesions. T_2-weighted MRI detected white matter lesions, independently of their T-cell content (W3 and W7-14dpi). However, this method failed to detect Fingolimod therapy response, as both demyelination and immune cells content influence the T_2 tissue properties, and are important components of lesions pre- and post-DMT (*27*). A major drawback of T_2-weighted MRI is the low sensitivity for grey matter lesion detection (*18,28*). In contrast, ^{18}F-FAraG PET detected changes in white and grey matter, and thus could help identify lesions invisible on T_2-weighted MRI (Figures 1-2, 6). T_1 contrast-enhanced MRI indicated BBB alterations following EAE immunization, as previously described (*29*), and detected Fingolimod efficacy as no BBB disruption was observed in treated animals, supporting Fingolimod's action on endothelial cells (*30*).

CONCLUSION

Altogether, our results indicate that ^{18}F-FAraG PET can be used to non-invasively image T-cell infiltration within the brain and spinal cord during a demyelinating event, and detects response to immunomodulatory therapy. These data support further investigation of ^{18}F-FAraG as a potential agent for clinical translation, with the aim to improve lesion characterization in MS patients and provide a novel tool to evaluate response to therapies.

DISCLOSURE

This work was supported by research grants: NIH R21AI153749, NIH R01NS102156, NMSS research grant RG-1701-26630, Hilton Foundation – Marilyn Hilton Award for Innovation in MS Research #17319 and the Dana Foundation: The David Mahoney Neuroimaging program. J. Levi is employed by CellSight Technologies. CellSight Technologies is commercializing ^{18}F-FAraG as a PET tracer for evaluation of immune response in immunotherapy. No other potential conflicts of interest relevant to this article exist.

ACKNOWLEDGEMENTS

We thank Yangjie Huang, PhD, Ning Zhao, PhD, Denis Beckford-Vera, PhD for their assistance with experiments and helpful discussion. We thank the UCSF Radiopharmaceutical Facility for the preparation of ^{18}F-FAraG.

KEY POINTS

Question

Can ^{18}F-FAraG PET imaging detect T-cell infiltration in the CNS in a preclinical model of MS and improve lesion characterization when combined with conventional MRI?

Pertinent Findings

^{18}F-FAraG uptake increases in brain and spinal cord of a MS mouse model and correlates with T-cell density, providing additional information on T-cells presence in MR detected lesions and enabling lesion stratification. Following treatment with a immunomodulatory DMT, ^{18}F-FAraG uptake was decreased in brain and spinal cord, highlighting its potential to monitor response to immunotherapy.

Implication for Patient Care

^{18}F-FAraG may provide a new methodology to evaluate T-cell presence in the CNS, and thus may enable patient stratification, monitoring of immune cell dynamics during disease progression and following therapy in MS and other T-cell mediated neurological conditions.

REFERENCES

1. Reich DS, Lucchinetti CF, Calabresi PA. Multiple sclerosis. *N Engl J Med.* 2018;378:169-180.

2. Pardo G, Jones DE. The sequence of disease-modifying therapies in relapsing multiple sclerosis: safety and immunologic considerations. *J Neurol.* 2017;264:2351-2374.

3. Lucchinetti C, Bruck W, Parisi J, Scheithauer B, Rodriguez M, Lassmann H. Heterogeneity of multiple sclerosis lesions: implications for the pathogenesis of demyelination. *Ann Neurol.* 2000;47:707-717.

4. Lucchinetti CF, Popescu BF, Bunyan RF, et al. Inflammatory cortical demyelination in early multiple sclerosis. *N Engl J Med.* 2011;365:2188-2197.

5. Kutzelnigg A, Lucchinetti CF, Stadelmann C, et al. Cortical demyelination and diffuse white matter injury in multiple sclerosis. *Brain.* 2005;128:2705-2712.

6. Barnett MH, Prineas JW. Relapsing and remitting multiple sclerosis: pathology of the newly forming lesion. *Ann Neurol.* 2004;55:458-468.

7. Marik C, Felts PA, Bauer J, Lassmann H, Smith KJ. Lesion genesis in a subset of patients with multiple sclerosis: a role for innate immunity? *Brain.* 2007;130:2800-2815.

8. Thompson AJ, Banwell BL, Barkhof F, et al. Diagnosis of multiple sclerosis: 2017 revisions of the McDonald criteria. *Lancet Neurol.* 2018;17:162-173.

9. Filippi M, Bar-Or A, Piehl F, et al. Multiple sclerosis. *Nat Rev Dis Primers.* 2018;4:43.

10. Levi J, Lam T, Goth SR, et al. Imaging of activated T cells as an early predictor of immune response to anti-PD-1 therapy. *Cancer Res.* 2019;79:3455-3465.

11. Ronald JA, Kim BS, Gowrishankar G, et al. A PET Imaging strategy to visualize activated T cells in acute graft-versus-host disease elicited by allogenic hematopoietic cell transplant. *Cancer Res.* 2017;77:2893-2902.

12. Franc BL, Goth S, MacKenzie J, et al. In vivo PET imaging of the activated immune environment in a small animal model of inflammatory arthritis. *Mol Imaging.* 2017;16:1536012117712638.

13. Namavari M, Chang YF, Kusler B, Yaghoubi S, Mitchell BS, Gambhir SS. Synthesis of 2'-deoxy-2'-[18F]fluoro-9-beta-D-arabinofuranosylguanine: a novel agent for imaging T-cell activation with PET. *Mol Imaging Biol.* 2011;13:812-818.

14. Levi J, Goth S, Huynh L, et al. (18)F-FAraG PET for CD8 profiling of tumors and assessment of immunomodulation by chemotherapy. *J Nucl Med.* 2020. "In press."

15. Ruther BJ, Scheld M, Dreymueller D, et al. Combination of cuprizone and experimental autoimmune encephalomyelitis to study inflammatory brain lesion formation and progression. *Glia.* 2017;65:1900-1913.

16. Brinkmann V. FTY720 (fingolimod) in multiple sclerosis: therapeutic effects in the immune and the central nervous system. *Br J Pharmacol.* 2009;158:1173-1182.

17. Guglielmetti C, Najac C, Didonna A, Van der Linden A, Ronen SM, Chaumeil MM. Hyperpolarized (13)C MR metabolic imaging can detect neuroinflammation in vivo in a multiple sclerosis murine model. *Proc Natl Acad Sci U S A.* 2017;114:E6982-E6991.

18. Guglielmetti C, Veraart J, Roelant E, et al. Diffusion kurtosis imaging probes cortical alterations and white matter pathology following cuprizone induced demyelination and spontaneous remyelination. *Neuroimage.* 2016;125:363-377.

19. James ML, Hoehne A, Mayer AT, et al. Imaging B cells in a mouse model of multiple sclerosis using (64)Cu-Rituximab PET. *J Nucl Med.* 2017;58:1845-1851.

20. Bettio LE, Gil-Mohapel J, Rodrigues AL. Guanosine and its role in neuropathologies. *Purinergic Signal.* 2016;12:411-426.

21. Pardridge WM. CNS drug design based on principles of blood-brain barrier transport. *J Neurochem.* 1998;70:1781-1792.

22. Chen BY, Ghezzi C, Villegas B, et al. (18)F-FAC PET visualizes brain-infiltrating leukocytes in a mouse model of multiple sclerosis. *J Nucl Med.* 2020;61:757-763.

23. Salas JR, Chen BY, Wong A, et al. (18)F-FAC PET selectively images liver-infiltrating CD4 and CD8 T cells in a mouse model of autoimmune hepatitis. *J Nucl Med.* 2018;59:1616-1623.

24. Radu CG, Shu CJ, Nair-Gill E, et al. Molecular imaging of lymphoid organs and immune activation by positron emission tomography with a new [18F]-labeled 2'-deoxycytidine analog. *Nat Med.* 2008;14:783-788.

25. Ntranos A, Hall O, Robinson DP, et al. FTY720 impairs CD8 T-cell function independently of the sphingosine-1-phosphate pathway. *J Neuroimmunol.* 2014;270:13-21.

26. Constantinescu CS, Farooqi N, O'Brien K, Gran B. Experimental autoimmune encephalomyelitis (EAE) as a model for multiple sclerosis (MS). *Br J Pharmacol.* 2011;164:1079-1106.

27. Barkovich AJ. Concepts of myelin and myelination in neuroradiology. *AJNR Am J Neuroradiol.* 2000;21:1099-1109.

28. Stadelmann C, Albert M, Wegner C, Bruck W. Cortical pathology in multiple sclerosis. *Curr Opin Neurol.* 2008;21:229-234.

29. Floris S, Blezer EL, Schreibelt G, et al. Blood-brain barrier permeability and monocyte infiltration in experimental allergic encephalomyelitis: a quantitative MRI study. *Brain.* 2004;127:616-627.

30. Zhao Y, Shi D, Cao K, et al. Fingolimod targets cerebral endothelial activation to block leukocyte recruitment in the central nervous system. *J Leukoc Biol.* 2018;103:107-118.

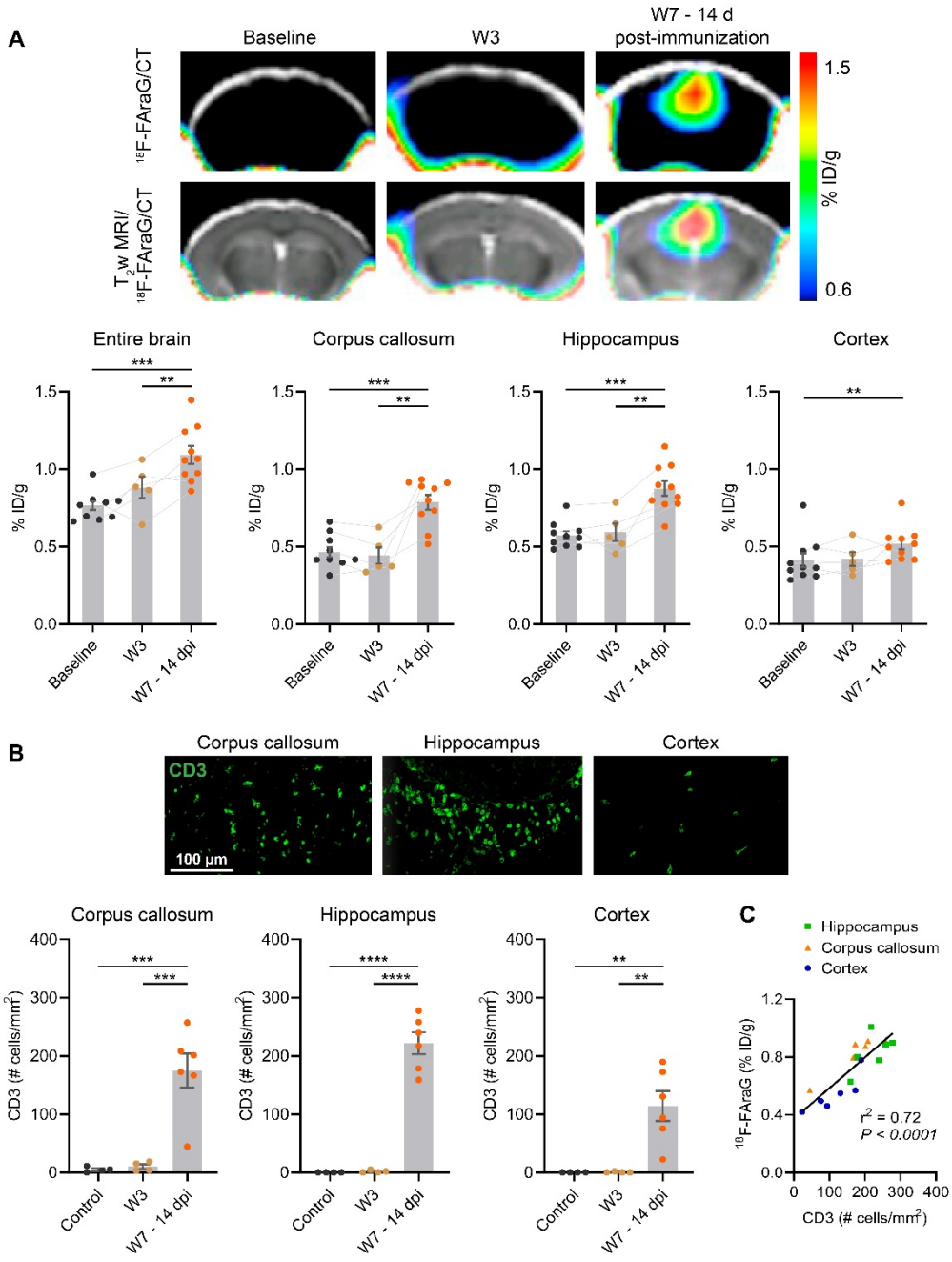

FIGURE 1. (A) ^{18}F-FAraG PET/ CT and ^{18}F-FAraG PET/ CT overlaid on T_2w MR images at Baseline, W3 and W7-14dpi. Graphs show ^{18}F-FAraG uptake in the entire brain, corpus callosum, hippocampus and cortex. (B) Immunofluorescence images of CD3 T-cells (green) from the corpus callosum, hippocampus and cortex at W7-14dpi. Quantification of CD3 T-cells in the corpus callosum, hippocampus and cortex at Baseline, W3 and W7-14dpi. (C) Correlation of ^{18}F-FAraG signal with CD3 T-cells at W7-14dpi, *$**p\leq0.01$, $***p\leq0.001$, $****p\leq0.0001$.

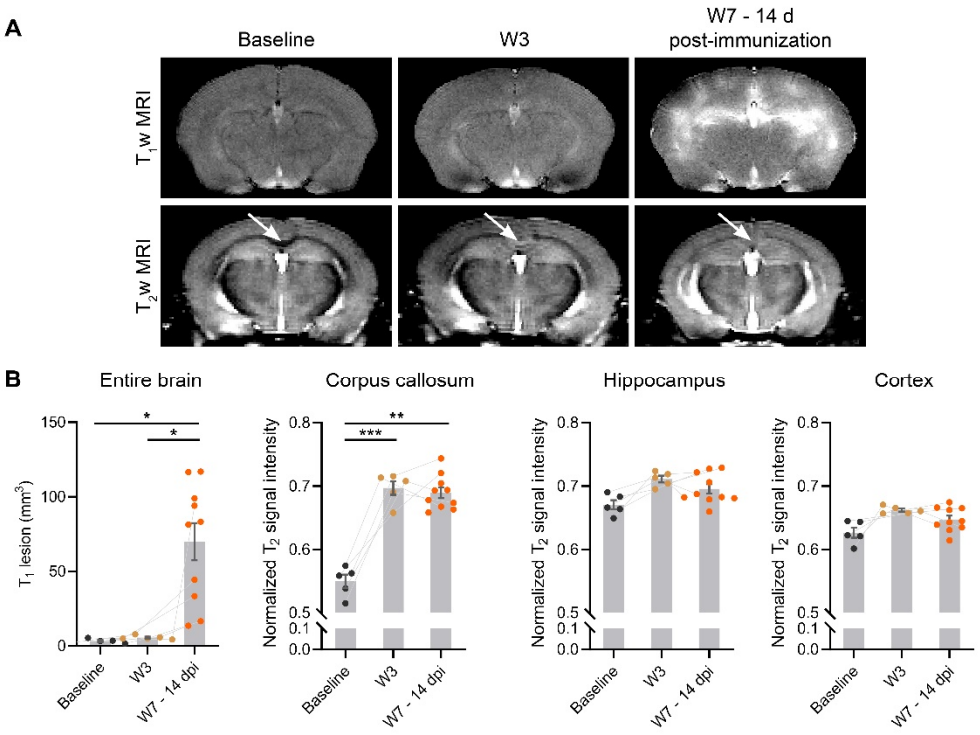

FIGURE 2. (A) T_1w MR images post injection of gadolinium and T_2w MR images at Baseline, W3 and W7-14dpi. Arrows indicate the corpus callosum. (B) Corresponding quantification of T_1 enhancing lesions and normalized T_2w signal intensity from the corpus callosum, hippocampus and cortex. *$*p\leq0.05$, $**p\leq0.01$, $***p\leq0.001$.

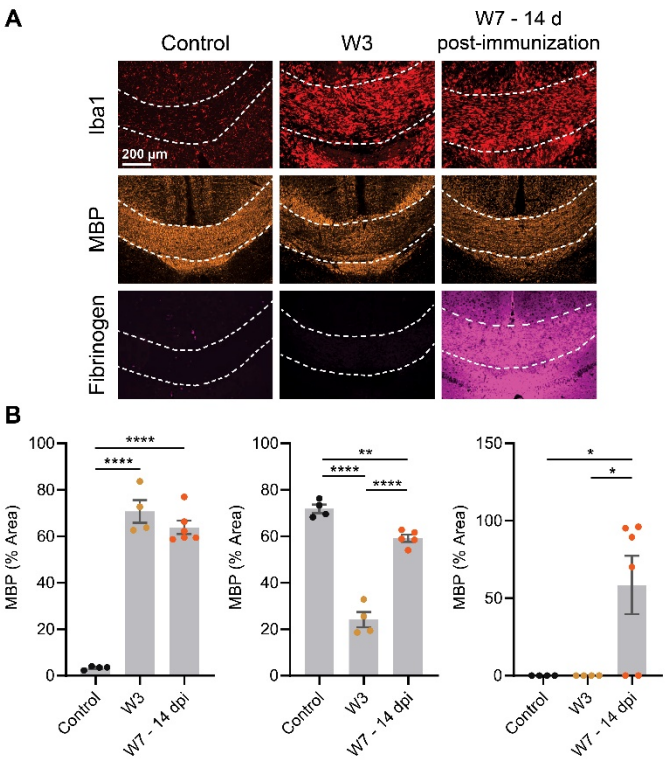

FIGURE 3. (A) Immunofluorescence images from the corpus callosum (dashed lines) for microglia/ macrophages (Iba1, red), myelin (MBP, orange) and fibrinogen (magenta), and (B) corresponding quantitative analyses in control animals, at W3 and W7-14dpi. *$p \leq 0.05$, **$p \leq 0.01$, ****$p \leq 0.0001$.

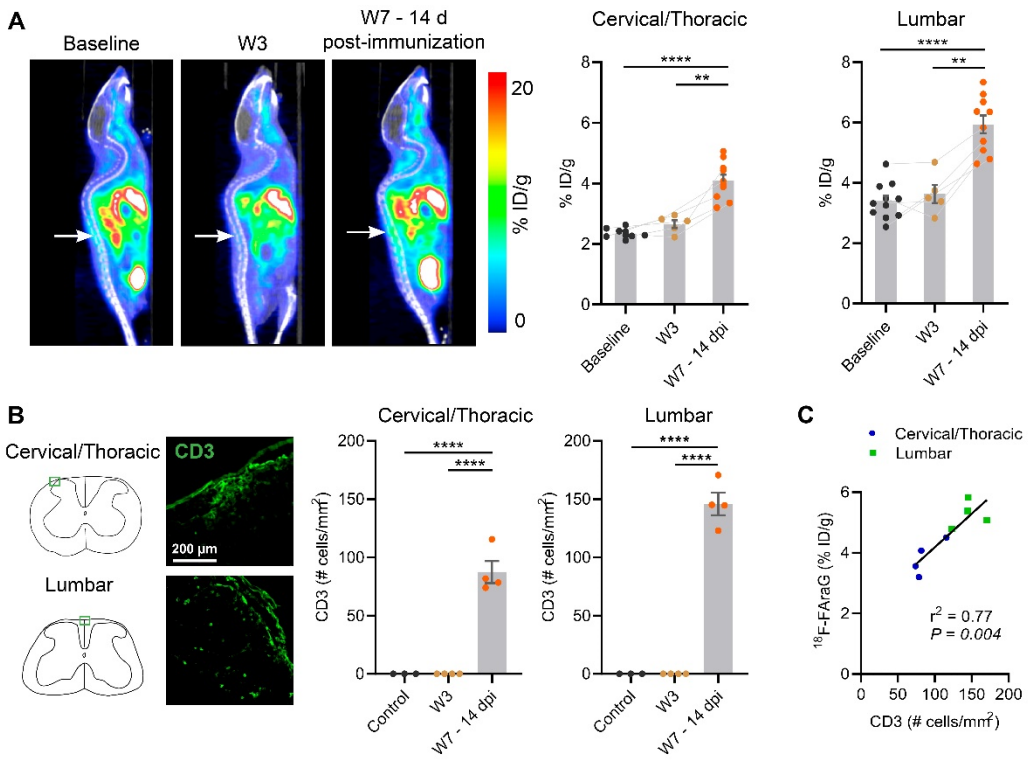

FIGURE 4. (A) ^{18}F-FAraG PET/ CT sagittal images at Baseline, W3 and W7-14dpi. White arrows point to the lumbar spinal cord. Graphs show corresponding quantification of ^{18}F-FAraG signal in the cervical/ thoracic, and lumbar spinal cord. (B) Immunofluorescence images of CD3 T-cells (green) in the cervical/ thoracic and lumbar spinal cord at W7-14dpi, and quantification of CD3 immunostaining at Baseline, W3 and W7-14dpi. (C) Correlation of ^{18}F-FAraG signal with CD3 T-cells at W7-14dpi. ***p≤0.01,* ****p≤0.0001*.

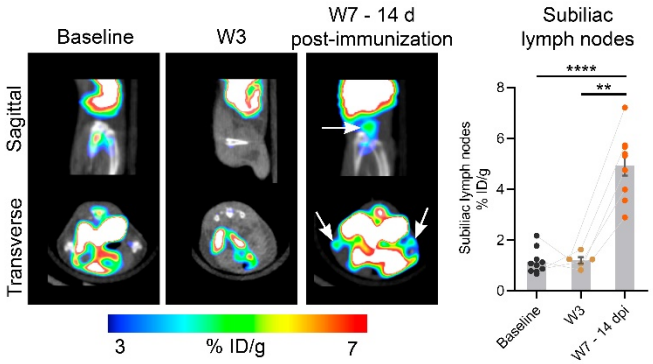

FIGURE 5. ^{18}F-FAraG PET/ CT images showing the subiliac lymph nodes and quantification of ^{18}F-FAraG uptake at Baseline, W3 and W7-14dpi. ***p≤0.01,* ****p≤0.0001*.

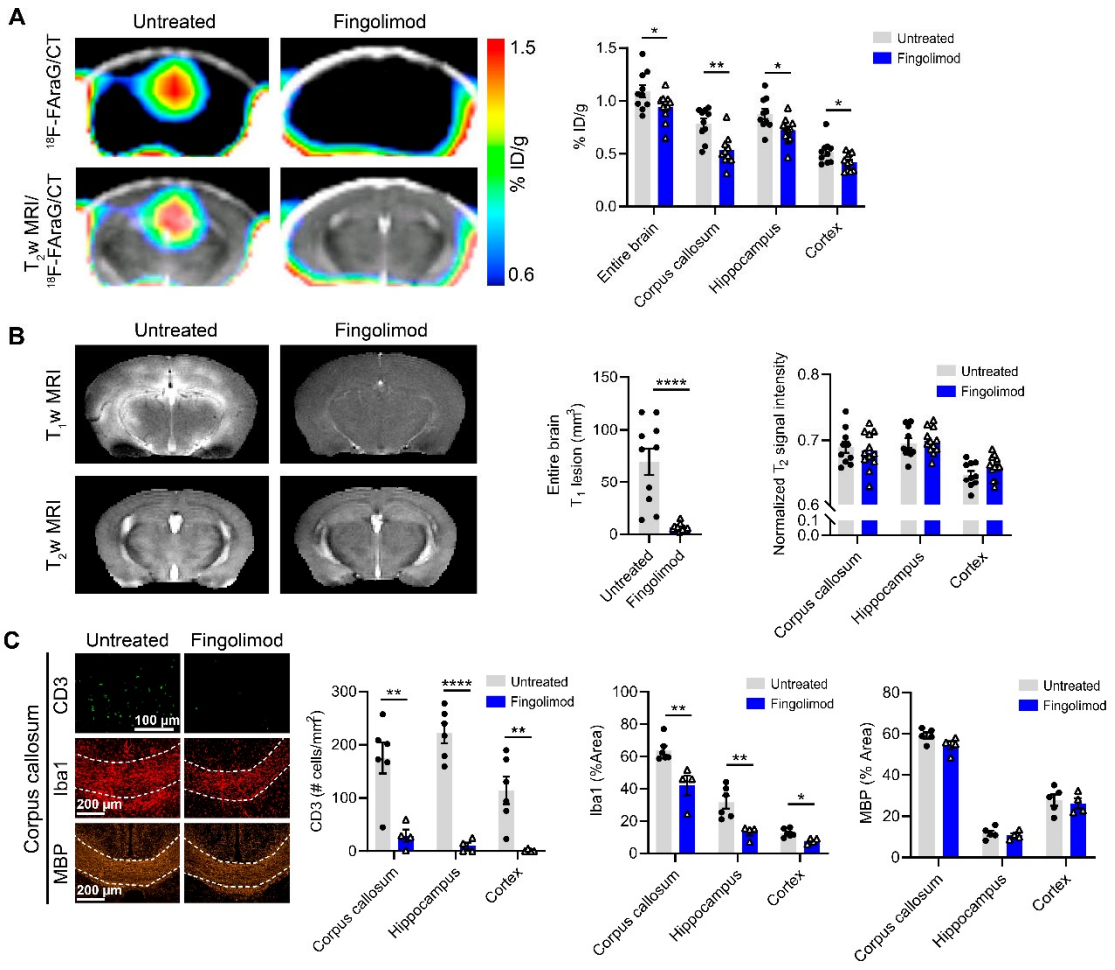

FIGURE 6. (A) ^{18}F-FAraG PET/ CT and ^{18}F-FAraG PET/ CT overlaid on T_2w MR images from untreated and Fingolimod-treated at W7-14dpi. Graph shows quantification of ^{18}F-FAraG signal in the entire brain, corpus callosum, hippocampus and cortex. (B) T_1w and T_2w MR images of Fingolimod-treated and untreated mice and corresponding quantification of T_1 enhancing lesions and normalized T_2w from the corpus callosum, hippocampus and cortex. (C) Immunofluorescence images of the corpus callosum for CD3 T-cells (green), microglia/ macrophages (Iba1, red), and myelin (MBP, orange) from untreated and Fingolimod-treated mice at W7-14dpi. Graphs show quantification of immunofluorescence images from the corpus callosum, hippocampus and cortex. *$p\leq0.05$, **$p\leq0.01$, ****$p\leq0.0001$.

Graphical Abstract

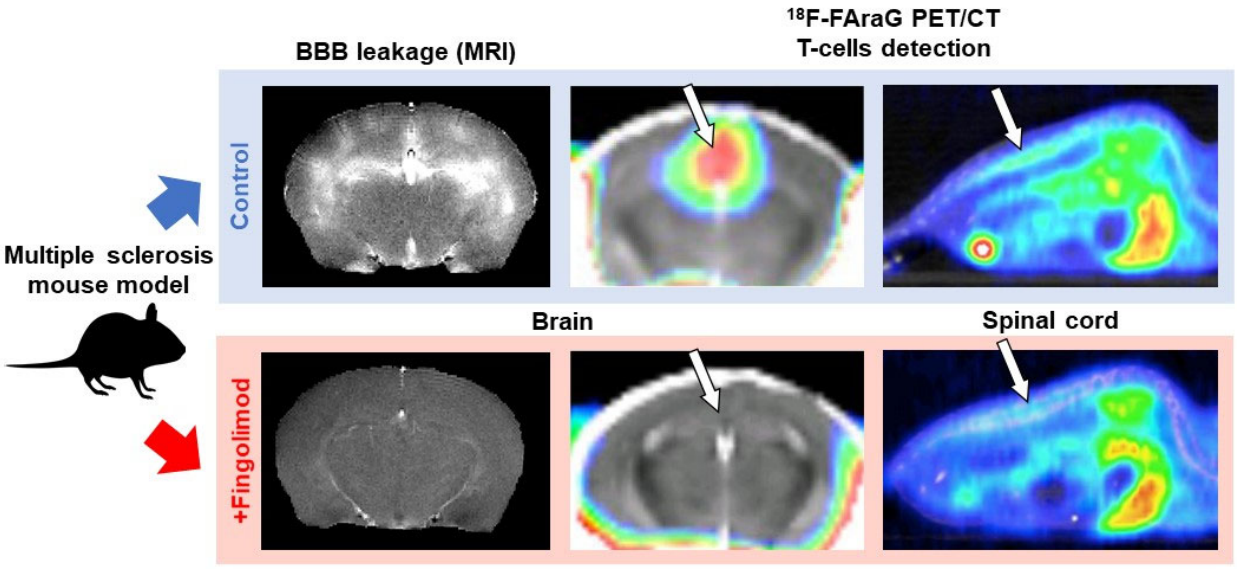

SUPPLEMENTAL INFORMATION

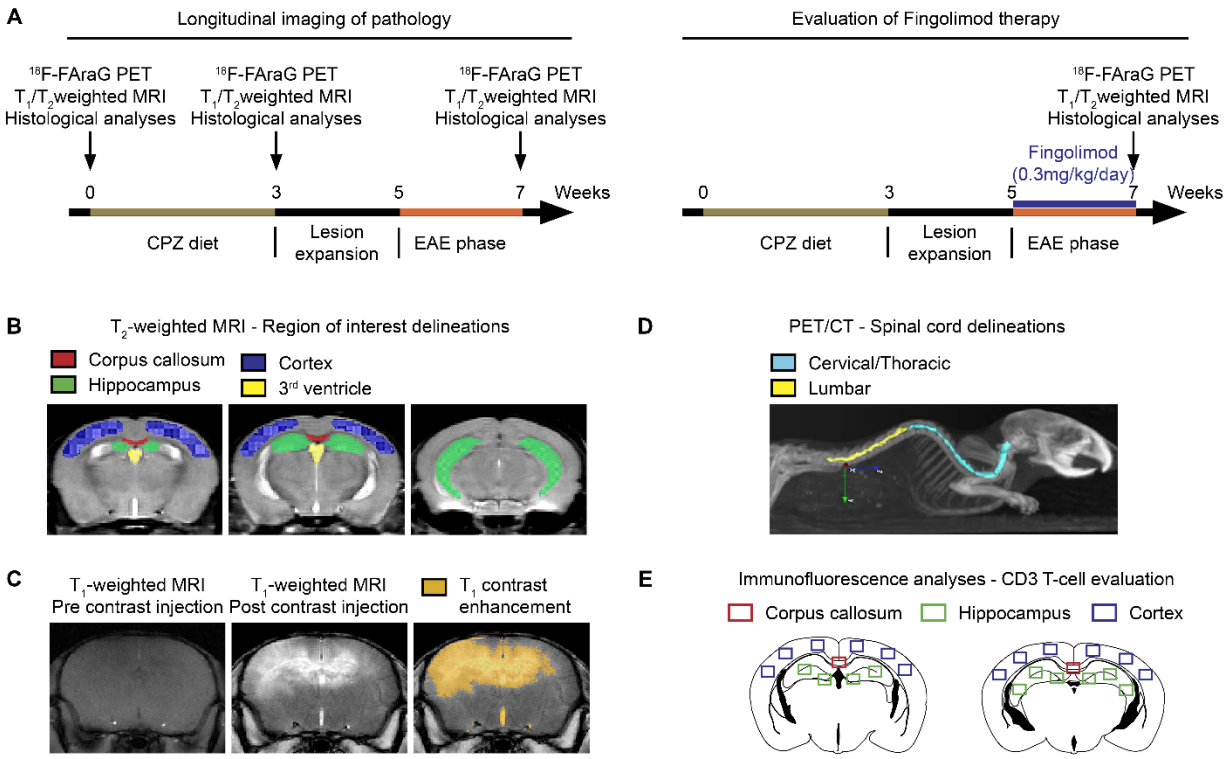

Supplemental Figure 1.

(A) Experimental outline indicates the timeline of the CPZ-EAE model induction, Fingolimod treatment, *in vivo* PET/ CT and MRI time points, and histological analyses. (B) Representative example of regions of interests (ROIs) delineated on T_2-weighted images for the corpus callosum (red), hippocampus (green), cortex (dark blue) and 3rd ventricle (yellow). (C) Representative T_1-weighted MR image obtained prior and after injection of gadolinium, and corresponding delineation of T_1 signal contrast enhancement (orange). (D) Representative CT image showing the delineation of the cervical/ thoracic (light blue) and lumbar (yellow) spinal cord segments. (E) Schematic illustration of brain regions used for evaluation of CD3 T-cell number in the corpus callosum (red, 2 regions), hippocampus (green, 8-10 regions) and cortex (dark blue, 10-12 regions).

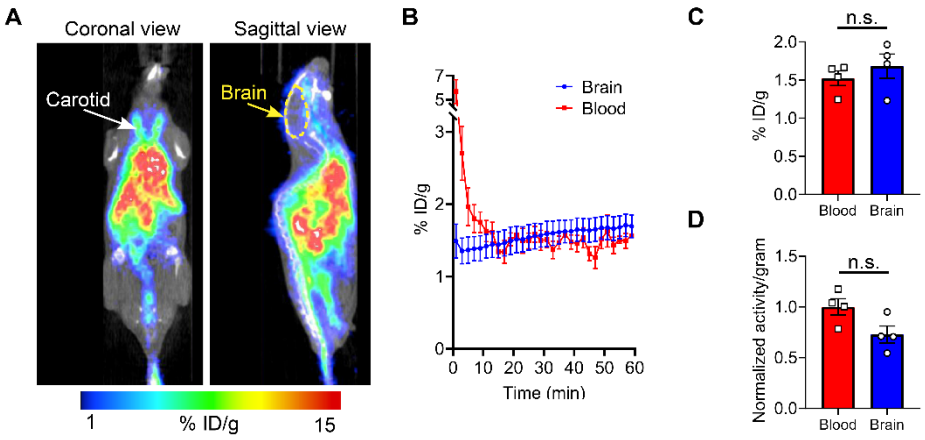

Supplemental Figure 2.

(A) Representative ^{18}F-FAraG PET/ CT image of a control mouse acquired during the first 2 minutes following iv injection of ^{18}F-FAraG. ^{18}F-FAraG signal can be detected in the left and right carotids (white arrow). The brain area used to measure ^{18}F-FAraG signal from the brain tissue is indicated by a dashed yellow line. (B) Time-activity curves from the blood and brain indicating steady accumulation of ^{18}F-FAraG into the brain tissue. (C) No significant differences were observed between ^{18}F-FAraG levels in the blood and brain, calculated from the averaged mean of the last 10 minutes of dynamic PET acquisition. Brain-to-blood ratio calculated from PET images is 1.1±0.2. (D) No significant differences were observed between the normalized blood and brain^{18}F-FAraG levels quantified from *ex vivo* biodistribution studies. Brain-to-blood ratio calculated from *ex vivo* biodistribution studies is 0.73±0.1. n.s. not significant.

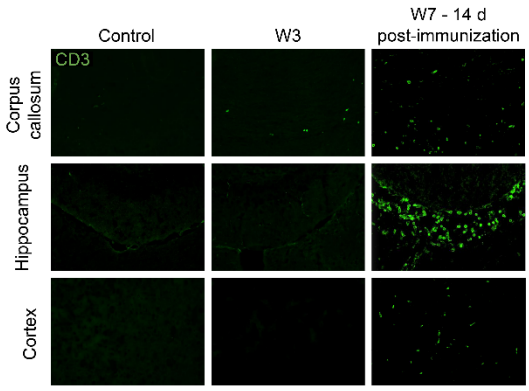

Supplemental Figure 3.

Representative immunofluorescence images showing low CD3 T-cells infiltration in the corpus callosum at W3, and elevated CD3 T-cells infiltration in the corpus callosum, hippocampus and cortex at W7.

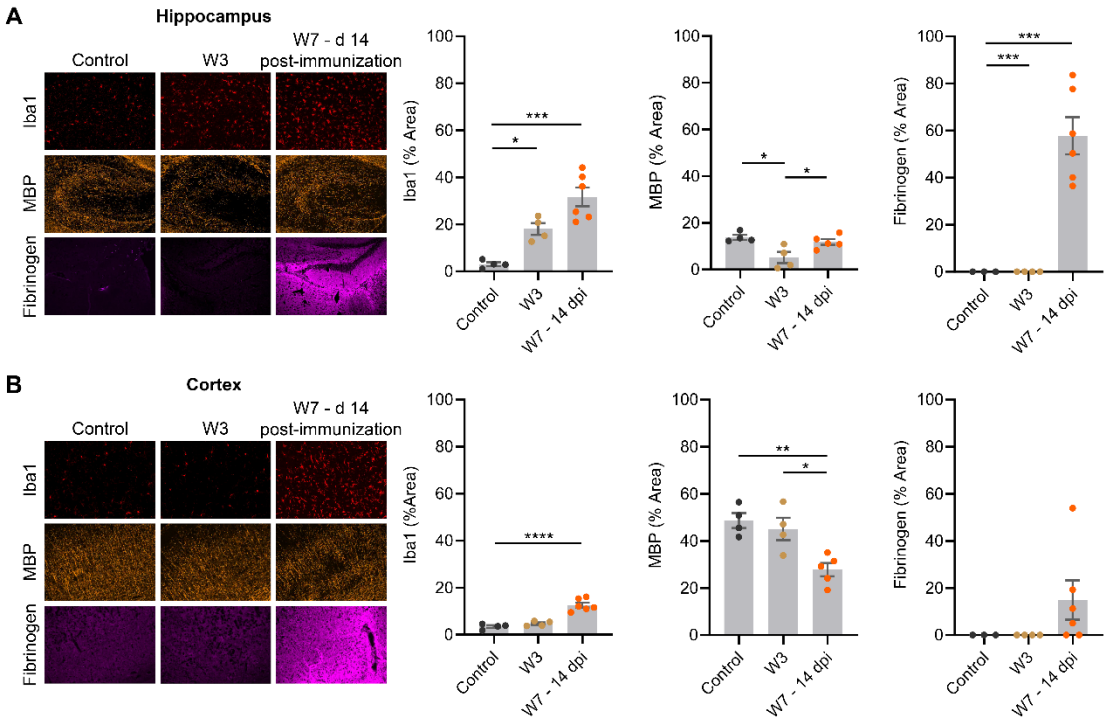

Supplemental Figure 4.

(A) Representative immunofluorescence images from the hippocampus in control animals, at W3 and W7 for microglia/ macrophages (Iba1, red), myelin basic protein (MBP, orange) and fibrinogen (pink). Quantitative analyses indicated a significant increase of microglia/ macrophages (Iba1) at W3 and W7. Demyelination was observed through a decrease of MBP at W3 only. Note that spontaneous remyelination occurred between W3 and W7. Important fibrinogen deposition was detected at W7 for all individuals. (B) Representative immunofluorescence images from the cortex in controls, at W3 and W7 for microglia/ macrophages (Iba1, red), myelin basic protein (MBP, orange) and fibrinogen (pink). Quantitative analyses indicated a significant increase of microglia/ macrophages (Iba1) at W7. Patchy cortical demyelination was observed at W7, and fibrinogen deposition was detected at W7 only in a subset of animals *(*p≤0.05, **p≤0.01, ***p≤0.001, ****p≤0.0001)*.

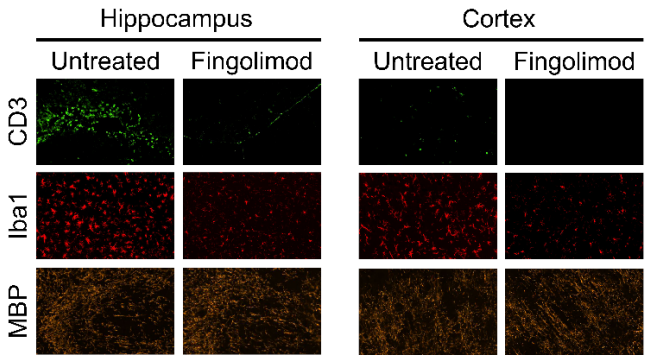

Supplementary Figure 5.

Representative immunofluorescence analyses of the hippocampus and cortex for untreated and Fingolimod-treated animals at W7 for CD3 T-cells (green), microglia/ macrophages (Iba1, red), and myelin basic protein (MBP, orange) showing lower number of CD3 T-cells and microglia/ macrophages in Fingolimod-treated compared to untreated mice, and no difference in myelin.

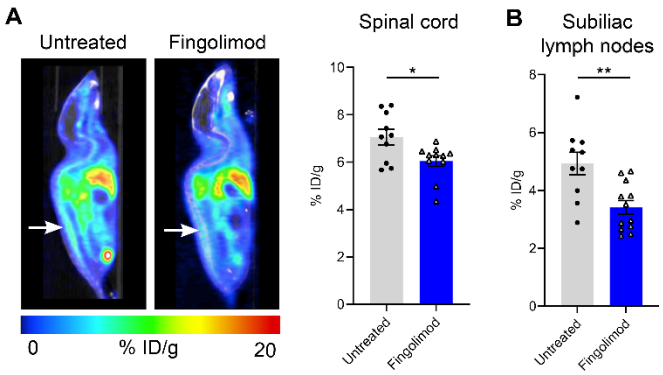

Supplemental Figure 6.

(A) Representative ^{18}F-FAraG PET/ CT images and quantitative analyses indicate lower ^{18}F-FAraG signal in the spinal cord (arrows) of Fingolimod-treated mice compared to untreated mice. (B) Similarly, quantitative analyses revealed significantly lower ^{18}F-FAraG signal in the subiliac lymph nodes of Fingolimod-treated mice compared to untreated mice *(*$p \leq 0.05$, **$p \leq 0.01$)*.

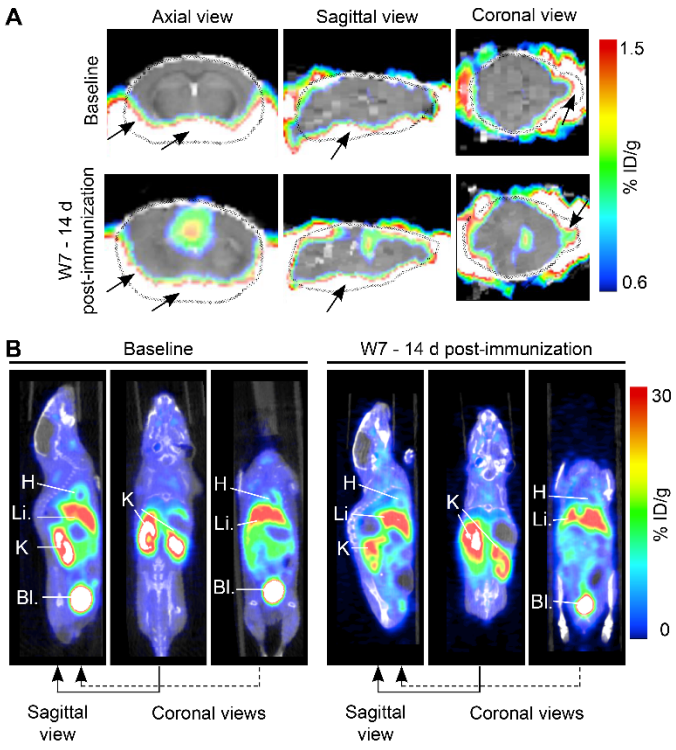

Supplemental Figure 7.

(A) ^{18}F-FAraG PET/ CT images overlaid on T_2w MR images showing different sections of the brain from a representative mouse at Baseline and W7-14dpi. ^{18}F-FAraG images indicate higher signal uptake in regions closer to the ventral part of the brain at Baseline and W7+14dpi (black arrows). (B) ^{18}F-FAraG PET/ CT images of the entire mouse body from a representative mouse at Baseline and at W7-14dpi showing accumulation of ^{18}F-FAraG in peripheral organs including liver (Li.), heart (H), kidneys (K) and bladder (Bl.).

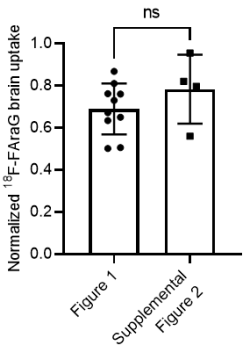

Supplemental Figure 8.

^{18}F-FAraG signal in the brain normalized to ^{18}F-FAraG signal in the leg muscles, shown for the two cohort of control mice (Figure 1 and Supplemental Figure 2). No statistical difference was found between the normalized ^{18}F-FAraG signal in the brain between these two cohorts of control mice (*p=0.2575*).

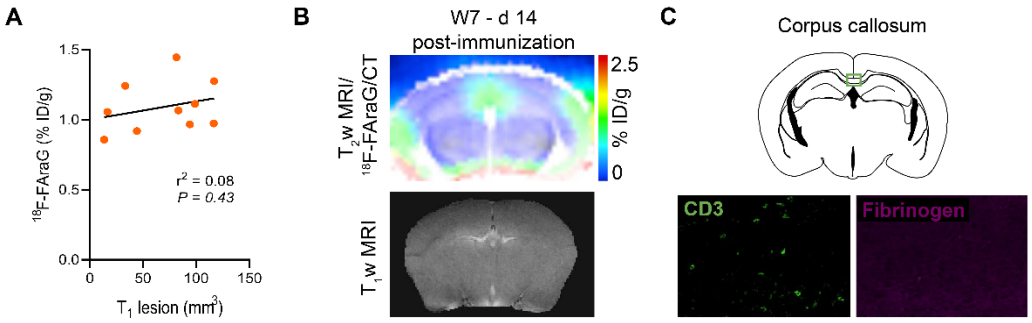

Supplemental Figure 9.

(A) ^{18}F-FAraG signal did not correlate to the T_1 enhancing lesion volume (r^2 = 0.08, *p = 0.43*). (B) Representative ^{18}F-FAraG PET/ CT overlaid on T_2w MRI and corresponding T_1w MRI indicating increased ^{18}F-FAraG signal in the corpus callosum but no T_1 enhancing lesion. (C) Corresponding immunofluorescence images confirmed the presence of CD3 T-cells in the corpus callosum and no BBB alteration indicated by no fibrinogen deposition.